



MOR nanosheets with tunable c-axis thickness and their catalytic performance in DME carbonylation

Kaipeng Cao^{a,d,1}, Wei Chen^{b,1}, Dong Fan^a, Zhenghao Jia^c, Nan Chen^{a,d}, Dali Zhu^a, Shutao Xu^a, Anmin Zheng^{b,e,*}, Peng Tian^{a,*}, Zhongmin Liu^{a,*}

^a National Engineering Research Center of Lower-Carbon Catalysis Technology, Dalian National Laboratory for Clean Energy, Dalian Institute of Chemical Physics, Chinese Academy of Sciences, Dalian 116023, China

^b State Key Laboratory of Magnetic Resonance and Atomic and Molecular Physics, National Center for Magnetic Resonance in Wuhan, Innovation Academy for Precision Measurement Science and Technology, Chinese Academy of Sciences, Wuhan 430071, China

^c Division of Energy Research Resources, Dalian Institute of Chemical Physics, Chinese Academy of Sciences, Dalian 116023, China

^d University of Chinese Academy of Sciences, Chinese Academy of Sciences, Beijing 100049, China

^e Interdisciplinary Institute of NMR and Molecular Sciences, School of Chemistry and Chemical Engineering, Wuhan University of Science and Technology, Wuhan, 430081, China

ARTICLE INFO

Keywords:
MOR zeolite
Nanosheets
Synthesis
Crystal growth
DME carbonylation

ABSTRACT

Controlling the anisotropic growth of crystals to achieve desired morphology is a challenge in zeolite crystallization, which often requires the use of bulky organic surfactants or additional crystal growth modifiers. Here, MOR crystals with tunable c-axis thickness (12-MR channel direction) were readily synthesized with commercial tetraethylammonium hydroxide (TEAOH) as an organic-structure directing agent (OSDA). It is revealed that the relative growth rates of different crystal faces of MOR zeolite can be tuned by the crystallization temperature and TEAOH amount in the developed gel system. Higher temperature and lower TEAOH concentration can effectively retard the growth of MOR crystals along the c-axis, yielding MOR nanosheets with short c-axis thickness (ca. 40 nm). Investigation on the crystallization process demonstrates that the crystal growth follows a particle attachment mechanism. Theoretical calculation was further employed to elucidate the c-axis thickness variation of MOR zeolite under different conditions. A kilogram-scale synthesis of MOR nanosheets has been realized with a 10 L autoclave, achieving high solid yield of 92 %. The MOR nanosheets, offering short 12-MR diffusion path, exhibit substantially enhanced catalytic activity and stability in the dimethyl ether (DME) carbonylation to methyl acetate reaction.

1. Introduction

Zeolites have been widely used in chemical industry [1–5] owing to their tunable acidity and high (hydro)thermal stability. The ordered microporous channels of zeolites endow them with unique selectivity [6–8]. However, the channels of molecular dimension may impose restrictions on mass transport, causing a decreased catalytic activity and stability [9–11]. To enhance mass transport in zeolites, two well-known strategies have been developed, i.e., i) introduction of meso-/macropores into the crystals [12–15], ii) synthesis of nanosized crystals [16–18]. However, both strategies generally involve the utilization of expensive mesopore-forming agents or additives, increasing the cost and

complicating the synthesis process. In addition, nanosized zeolites are hard to be collected by filtration or centrifugation due to its ultra-small particle size. Alternatively, preparation of 2-dimensional (2D) or quasi-2D crystals with limited crystal growth in the direction along channels of interest is another effective approach to improve diffusion behaviors [19–22]. Considerable efforts have been devoted to 2D zeolite synthesis, particularly 2D ZSM-5, predominantly via the employment of designed bulky organic surfactants or organic structure directing agents (OSDAs) [23–27].

MOR zeolite is an important member of zeolite family that has received significant attention in recent years due to its excellent performances in dimethyl ether (DME) carbonylation [28], syngas/

* Corresponding authors at: State Key Laboratory of Magnetic Resonance and Atomic and Molecular Physics, National Center for Magnetic Resonance in Wuhan, Innovation Academy for Precision Measurement Science and Technology, Chinese Academy of Sciences, Wuhan 430071, China.

E-mail addresses: zhengam@wipm.ac.cn (A. Zheng), tianpeng@dicp.ac.cn (P. Tian), zml@dicp.ac.cn (Z. Liu).

¹ These authors contributed equally.

<https://doi.org/10.1016/j.cej.2024.150344>

Received 17 October 2023; Received in revised form 7 March 2024; Accepted 10 March 2024

Available online 12 March 2024

1385-8947/© 2024 Elsevier B.V. All rights reserved.

methanol to ethylene[7,29,30], and low-temperature oxidation of methane to methanol[31,32], as well as selective gas adsorption[33,34]. In particular, the zeolite-catalyzed DME carbonylation process has realized its industrialization in 2017, which offers a novel route to produce methylacetate (MAC) and its hydrogenation product ethanol from natural gas and coal. The MOR framework consists of 12-MR and elliptical 8-MR channels along the c-axis, connected by 8-MR side pockets along the b-axis[6,35]. As molecules can only enter through the 12-MR channels, MOR is commonly regarded as a unidimensional zeolite. It has been demonstrated that the mass transfer limitation in MOR zeolite could significantly inhibit reaction activity and stability [11,36], despite its relatively superior performance in reactions such as DME carbonylation. Therefore, MOR crystals with truncated c-axis dimension and hence shortened diffusion length are highly desired.

Although extensive efforts have been devoted to the morphology control of MOR zeolite, the tailored synthesis of 2D MOR nanosheets with truncated c-axis length, remains a challenge[35,37–43]. The employment of expensive organic surfactants and/or designed OSDAs is common, and in most cases, the a-axis and b-axis crystal lengths have been shortened with limited improvement of diffusion[42,44,45]. To the best of our knowledge, only Shen et al.[46] and Shvets et al.[40] synthesized MOR nanosheets with shortened c-axis crystal length under the assistance of specially designed bulky bifunctional surfactants, difficult for the scale-up production due to the high cost. On the other hand, numerous researches have demonstrated that a variety of synthetic parameters, including charge-balancing cations, mineralization agents, silica/alumina sources and crystallization conditions, can also affect the growth habits of zeolite materials[47]. Yet, it is still challenging to rationally control the morphology of zeolites due to the lack of in-depth understanding of their growth habits under specific conditions, which is also the case for MOR zeolite.

In this work, we report a mesopore-free approach for the synthesis of MOR nanosheet assemblies with short c-axis length (12-MR channel direction) by using commercial TEOAH as an OSDA. The crystal thickness along the c-axis can be facilely tuned in the range of 40 nm to 800 nm by controlling the OSDA concentration and crystallization temperature. On the basis of designed experiments and theoretical calculation, the intrinsic reason for the oriented growth habits of MOR crystals was elucidated. The obtained MOR nanosheets afford an enhanced catalytic activity and stability in the DME carbonylation reaction.

2. Experimental section

2.1. Materials and reagents

Sodium hydroxide (NaOH, 99.9 wt%, Shanghai Aladdin Industrial Co.); sodium aluminate (NaAlO_2 , 36.6 wt% Na_2O , 47.6 wt% Al_2O_3 , 15.8 wt% H_2O , Tianjin Guangfu Chemical Co.); silica sol (27.5 wt% SiO_2 , 72.5 wt% H_2O , Qingdao Chengyu Chemical Co.); tetraethylammonium hydroxide (TEAOH, 35 wt% in H_2O , Shanghai Annaiji Chemical Reagent Co.); tetramethylammonium hydroxide (TMAOH, 25 wt% in H_2O , Shanghai Annaiji Chemical Reagent Co.); hexamethyleneimine (HMI, 98 wt%, Shanghai Annaiji Chemical Reagent Co.); triethylamine (TEA, 99 wt%, Tianjin Damao Chemical Reagent Co.); pseudoboehmite (67 wt% Al_2O_3 , 33 wt% H_2O); phosphoric acid (85 wt% H_3PO_4 , 15 wt% H_2O , Sichuan Xianfeng Chemical Co.), commercial MOR (Si/Al = 12, ZR CATALYST Co., Ltd.); reactant gas ($\text{DME}/\text{CO}/\text{N}_2 = 5/35/60$, Dalian Guang Ming Special Gas Co., Ltd.).

2.2. Zeolites synthesis and catalyst preparation

A hydrothermal synthesis method was carried out for the preparation of MOR zeolites. NaOH, NaAlO_2 , OSDA (TEAOH or HMI), and H_2O were first introduced into a beaker at room temperature and stirred until dissolved completely. Silica sol was then introduced in drops under

intense agitation. Subsequently, commercial MOR zeolite used as seeds (4 wt% relative to SiO_2) was added into the above mixture. The specific compositions of the synthetic gel have been shown in Table S2-S6. After aging for 1 h under stirring, the final gel was transferred into an autoclave (100 mL) and heated under tumbling conditions (details for specific gel ratio and crystallization conditions are shown in SI). Afterwards, the crystallized product was centrifuged for recovery, washed with distilled water and dried at 120 °C.

For the scale-up synthesis of MOR-P, a gel with molar composition of $1\text{SiO}_2: 1/33\text{Al}_2\text{O}_3: 0.2\text{NaOH}: 0.07\text{TEAOH}: 16.7\text{H}_2\text{O}$ with the addition of 4 wt% MOR seeds was carried out. In detail, 96.41 g NaAlO_2 , 74.48 g NaOH and 441 g TEOAH solution were added to 1821 g deionized water, to form a clear solution. 3292 g silica sol was slowly added into the clear solution under stirring. 36 g MOR seeds were added into the gel and then aged for 1 h under strong agitation at room temperature. The final mixture was charged into a 10 L stainless steel Parr autoclave, which was then sealed and heated up to 190 °C in 120 min. The crystallization was conducted under stirring (100 rpm) at 190 °C for 13 h. After crystallization, the product was centrifuged for recovery, washed with distilled water and dried at 120 °C.

For the synthesis of OFF zeolites, KOH, Al_2O_3 , TEOAH, TMAOH and H_2O were introduced into a beaker in sequence and stirred until dissolved completely. Silica sol was then introduced under intense agitation. The molar compositions of the synthetic gels have been shown in Table S8. After aging for 1 h under stirring, the final gel was transferred into an autoclave and heated under static conditions. Afterwards, the crystallized product was centrifuged for recovery, washed with distilled water and dried at 120 °C.

For the synthesis of SAPO-5, pseudoboehmite was added into a solution containing phosphoric acid and water under stirring. The mixture was stirred for 5 h, and then silica sol was added into the mixture and stirred for 30 min. After further addition of TEA, the resulting mixture was transferred into an autoclave, which was heated to crystallization temperature and kept at the designed temperature for 24 h under rotation. After the crystallization, the solid product was centrifuged for recovery, washed with distilled water and dried at 120 °C.

In order to obtain H-type zeolite samples, the as-made samples were first calcined at 550 °C. Subsequently, the calcined samples were ion-exchanged with NH_4NO_3 solution (1 mol/L, 80 °C for 1 h). The ion-exchange procedure was repeated three times and dried at 120 °C. Finally, the exchanged sample was calcined at 550 °C for 4 h under dry air.

2.3. Characterization

X-ray diffraction (XRD) patterns were obtained on an X-ray diffractometer of PANalytical X'Pert PRO with $\text{Cu K}\alpha$ radiation operating at 40 kV and 40 mA (scanning region: 5 ~ 50°). The relative crystallinity of the samples was calculated according to the sum of the peak height at $2\theta = 9.78^\circ$, 19.73° and 22.40° . For each recipe, the sample with the highest values was defined as standard sample with a relative crystallinity of 100 %. The morphologies of zeolites were acquired using Hitachi SU8020 scanning electron microscope (SEM). Selected area electron diffraction (SAED) patterns were taken from JEOL JEM-2100 transmission electron microscopy (TEM). High-angle annular dark-field-scanning transmission electron microscopy (HAADF-STEM) and integrated differential phase contrast (iDPC) images were recorded on FEI Titan Cubed Themis ETEM G3 300. The 4-quadrant DF4 detector were used to acquire the iDPC-STEM image. The convergence semi-angle for the iDPC image is 9.8 mrad and the collection semi-angle is 2–14 mrad. The probe current is ~ 1 pA. The dwell time is 2.5 $\mu\text{s}/\text{pixel}$, pixel size is 0.184 Å and the calculated dose is ~ 460 $\text{e}^-/\text{Å}^2$. The HAADF-STEM images were acquired with 10–63 mrad collection semi-angle and 0.184 Å² pixel size. Textural properties of the samples were obtained on a Micromeritics ASAP 2020 analyzer through N_2 adsorption and desorption measurements. Thermal analysis were determined on a TA Q-

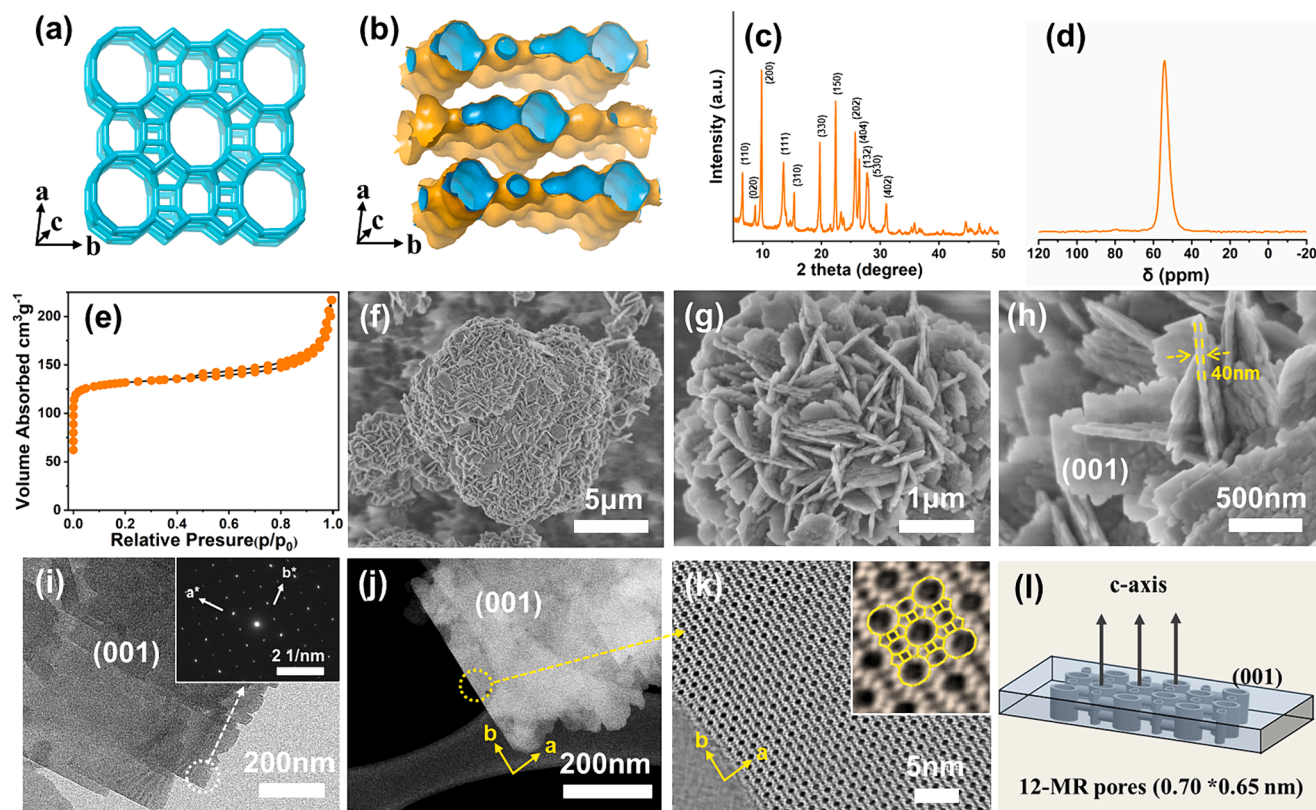


Fig. 1. General features of MOR nanosheets (MOR-P) obtained in the 1SiO₂: 1/33Al₂O₃: 0.2NaOH: 0.07TEAOH: 16.7H₂O system (190 °C, 15 h). (a) Framework of MOR zeolite viewed along [001]; (b) the pore system in the MOR crystal; (c) XRD pattern; (d) ²⁷Al MAS NMR spectrum; (e) N₂ physisorption isotherm; (f, g, h) SEM images of the MOR-P; (i) TEM image and SAED pattern; (j) HAADF-STEM image and (k) iDPC-STEM image of the MOR-P taken along the c-axis; (l) Illustration of the channel system in MOR-P.

600 thermogravimetric analyzer (TG). The bulk Si/Al ratios were measured on an X-ray fluorescence (XRF) spectrometer of Philips Magix-601. The temperature-programmed desorption of ammonia (NH₃-TPD) was performed using 100 mg powder of samples on Micromeritics AutoChem II 2920 equipped with a thermal conductivity detector. Prior to the measurement, the sample was pretreated under He flow at 450 °C for 1 h. The adsorption of NH₃ was carried out at 100 °C, which was followed by desorption from 100 to 700 °C. A Bruker Tensor 27 spectrometer (MCT detector) was adopted for the measurement of fourier transform infrared spectra (FTIR). The MOR samples were pressed self-supported wafers and placed into the in situ quartz cell. Subsequently, the wafers were dehydrated at 400 °C in a vacuum for 30 min to remove the water physisorbed. After cooling to room temperature, the spectra were collected by a MCT detector in the range of 400–4000 cm⁻¹ with a resolution of 4 cm⁻¹. ²⁷Al and ²⁹Si MAS NMR spectra were recorded on a Bruker Avance III 600 MHz spectrometer. ²⁷Al spectra were collected at 156.4 MHz with a spinning rate of 12 kHz, a recycle delay of 2 s and $\pi/8$ pulse width of 0.75 μ s. ²⁹Si spectra were recorded at 119.2 MHz with a $\pi/4$ pulse width of 2.5 μ s, a 10 s recycle delay and an 8 kHz spinning rate. The liquid ¹³C NMR analysis was performed on Bruker Avance III 400 using D₂O as deuterated reagent. Before NMR analysis, the as-synthesized sample was dissolved by 50 wt% HF acid solution (Mass zeolite/HF_{solution} = 1/8), and the liquids were analyzed.

2.4. Computational method

To obtain the distribution of TEA⁺ in MOR slab, Monte Carlo method was firstly employed to obtain the distribution of TEA⁺ in the unit cell of bulk MOR zeolite. Subsequently, 2D slab of 96 T was created by building supercell and deleting the atoms at the cell edge, and the three slabs of (001), (010) and (100) faces were established with at least 15 Å

vacuum layer. The slab was terminated with –OH groups, and OSDAs at the surface of slab were kept unchanged. The loading of TEA⁺ and the number of –OH groups in the slab were summarized in Table S7. Based on the constructed slab (slab_{TEA⁺}) containing OSDAs, the empty slab (slab) was created by deleting all OSDAs. To calculate the binding energy between slab and OSDA, the geometrical structures of two kinds of slabs (slab_{TEA⁺} and slab) were fully optimized by density functional theory (DFT) method, PBE functional[48] with Grimme's dispersion correction (DFT-D)[49] was used and all atoms were described by DNP basis set by DMOL3 software.[50].

The interaction energy (ΔE) was calculated by the formula:

$$\Delta E = (E_{slab_TEA^+} - E_{slab} - n \cdot E_{TEA^+}) / n$$

E_{slab_OSDA} , E_{slab} and E_{OSDA} are the energy of optimized structures of slab_{TEA⁺}, slab, and TEA⁺, n is the number of OSDA in slab_{TEA⁺}. Herein, the MOR_{slab} is all silicon to avoid the complicate discussion to Al distributions, especially multiple Al atoms in a slab, and thus both slab_{TEA⁺} and TEA⁺ are positively charged, which may lead to the underestimation of binding energy (ΔE) due to the ignoration of charge transfer between slab and TEA⁺, but it will not change the qualitative relationship of different slabs on ΔE .

2.5. Catalysis test

The DME carbonylation activity and stability of catalysts were evaluated in a fixed bed reactor (diameter = 8 mm). The H-MOR samples (0.25 g, 40–60 mesh) were pretreated with N₂ in the reactor at 400 °C for 2 h. Afterwards, the temperature was cooled to reaction temperature (200 °C), and a mixture of reactant gas (DME/CO/N₂ = 5/35/60) was introduced. The reaction was carried out at 2.0 MPa with a GHSV of 3600 mL/g/h. The products analysis was carried out using an Agilent

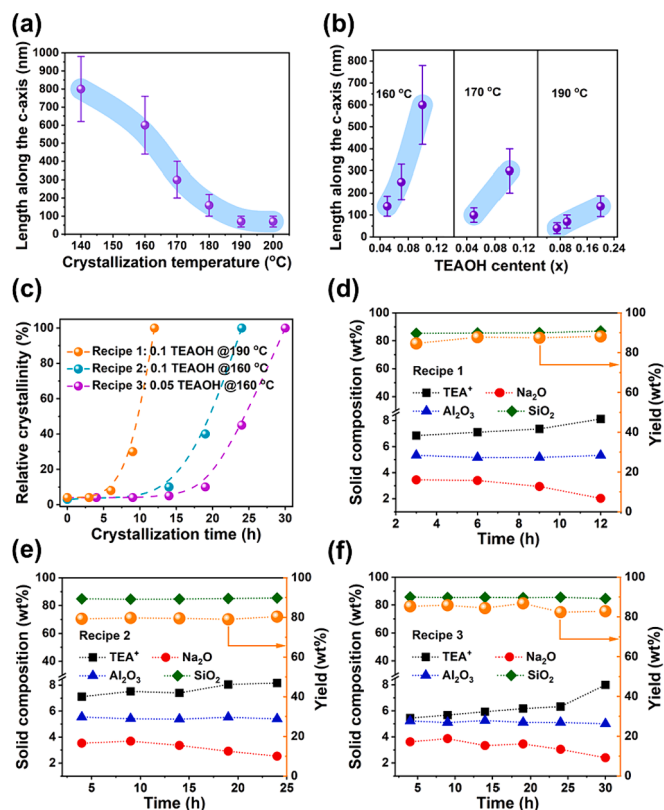


Fig. 2. Effect of (a) crystallization temperature and (b) TEOAH amount on the c-axis thickness of MOR zeolites. (c-f) The evolution of relative crystallinity, solid yields, normalized solid inorganic elemental compositions (measured by XRF), and OSDA contents (measured by TG) in the systems of Recipes 1–3. The gel molar composition for syntheses is $1\text{SiO}_2: 1/33\text{Al}_2\text{O}_3: 0.2\text{NaOH}: x\text{TEAOH}: 16.7\text{H}_2\text{O}$. For (a), $x = 0.1$. For Recipe 1, 2 and 3 in (c-f), $x = 0.1$ (190°C), 0.1 (160°C) and 0.05 (160°C), respectively.

7890B gas chromatograph equipped with Pora PLOT Q capillary column and FID detector.

3. Results and discussion

3.1. Synthesis of MOR nanosheets and the control of their c-axis thickness

Considerable synthesis efforts have been conducted to tune the crystal morphology of zeolite MOR by changing the gel compositions and crystallization conditions. MOR nanosheets (named MOR-P, Fig. 1) were obtained in high yield (~90 %) from an initial gel with molar composition of $1\text{SiO}_2: 1/33\text{Al}_2\text{O}_3: 0.2\text{NaOH}: 0.07\text{TEAOH}: 16.7\text{H}_2\text{O}$ after crystallization at 190°C for 15 h under tumbling conditions. The XRD pattern of the sample shows characteristic reflections of zeolite MOR with high crystallinity (Fig. 1c). ^{27}Al MAS NMR spectrum in Fig. 1d evidences the absence of octahedrally coordinated aluminum species, which are related to extra-framework aluminum. The bulk Si/Al ratio was measured to be 14.0 (XRF), similar to the framework Si/Al ratio (13.4) derived from ^{29}Si MAS NMR spectrum (Fig. S1). ^{13}C MAS NMR spectrum confirms the intact presence of TEA^+ in the micropores of MOR-P (Fig. S1). N_2 physisorption analysis of the calcined sample gives type I physisorption isotherm, with a micropore volume of $0.17\text{ cm}^3/\text{g}$ and BET surface area of $423\text{ m}^2/\text{g}$ (Fig. 1e, Table S1). A microscopy study shows that the MOR-P has a morphology of nanosheet assemblies (Fig. 1f-h and Fig. S2). The nanosheets have a thickness of around 40 nm with length and width dimensions in micrometer scale. Corresponding selected area electron diffraction (SAED) pattern reveals that the shortest dimension of the crystals runs along the c-axis (Fig. 1i). The 12-

MR pores of the MOR-P nanosheets can be clearly identified from iDPC-STEM image in Fig. 1k. These results demonstrate that MOR nanosheets with high crystallinity and impressive thickness of ca. 40 nm along the c-axis has been prepared by one-pot method without using bulky surfactants or modifiers.

A systematic investigation of the influence of synthetic conditions on the morphology of MOR zeolite was carried out based on a gel system of $1\text{SiO}_2: 1/33\text{Al}_2\text{O}_3: 0.2\text{NaOH}: 0.1\text{TEAOH}: 16.7\text{H}_2\text{O}$ (Table S2-S6, Fig. S3-S9). One of the important parameters for the achievement of MOR nanosheets is found to be the crystallization temperature. The MOR crystals present a gradually decreased thickness along the c-axis from more than eight hundreds to several tens of nanometers, when the temperature rises from 140°C to 190°C (Fig. 2a, S3, Table S2). Meanwhile, no substantial variation is observed for the crystal length along the a-axis and b-axis, resulting in a dramatic change of crystal morphology from rod-like shape to nanosheet shape. Further increasing the crystallization temperature to 200°C , impurities start to appear, and the crystal thickness doesn't show appreciable decrease.

The impact of OSDA amounts on the anisotropic growth of MOR crystals has never been reported in previous works. Herein, it is interesting to show that the increase of TEOAH amount has a negative effect on the crystal thickness, which is independent of crystallization temperature (Fig. 2b, S4, Table S3). However, excessively low TEOAH usage is not favorable for the synthesis of pure MOR phase. When the x ($\text{TEAOH}/\text{SiO}_2$) falls to 0.05, impurities start to occur. In addition, the effect of NaOH amount (Table S4, Fig. S5) is also examined. In the investigated range of $\text{NaOH}/\text{SiO}_2 = 0.16 \sim 0.22$, the change in NaOH amount shows little impact on the crystal thickness. Fig. S6 summarizes the variation of crystal thickness along the c-axis with the gel alkalinity. The inconsistent trends between two curves imply that gel alkalinity is not the crucial factor in determining the crystal thickness. It is speculated that the concentration of TEA^+ cation may be more important for tuning the anisotropic growth of MOR crystals, which was further evidenced by designed experiments. As shown in Table S5 and Fig. S7, the MOR crystal thickness presents an obviously increasing trend following the addition of TEACL. Additionally, the MOR nanosheets are not strictly constrained by gel Si/Al ratio. Its variation in the range of 12.5 to 38.5 can deliver pure MOR product with nanosheets morphology (Table S6, Fig. S8). Fig. S9 further displays the effect of seed amounts on the products. Without the addition of seeds, the gel with the same composition as that of Recipe 1 cannot yield pure MOR product. Following the increase of seed amounts (2–8 wt%), a gradually shortened time for complete crystallization can be observed, but it does not yield significant impact on the c-axis thickness of crystals.

3.2. Formation mechanism of MOR nanosheets

To learn the formation mechanism of MOR nanosheets and understand the intrinsic reason of crystallization temperatures and OSDA amounts in affecting the crystal thickness, three synthetic recipes were chosen and studied comparatively. The crystallization curves of the three systems are shown in Fig. 2c. They all present similar crystallization process with the existence of induction period and fast crystal growth period. Both higher temperature and larger TEOAH amounts are helpful for the shortening of induction period and the acceleration of crystal growth. From Fig. 2d-f, the three systems have high yields of more than 80 % with little fluctuation during the entire crystallization period. The contents of silica and alumina in solid phase are barely changed, while the contents of equilibrium cations (TEA^+ and Na^+) show an opposite variation trend with the crystallization of zeolite MOR. More TEA^+ cations are gradually incorporated into the solid phase with the discharge of Na^+ .

The intermediate solids were further inspected by SEM and TEM (Fig. 3 and Fig. S10-S13). μm -sized amorphous materials consisting of tiny particles are formed at the very initial stage of all three systems. As the crystallization proceeds, for Recipe 1, small plate-like crystals start

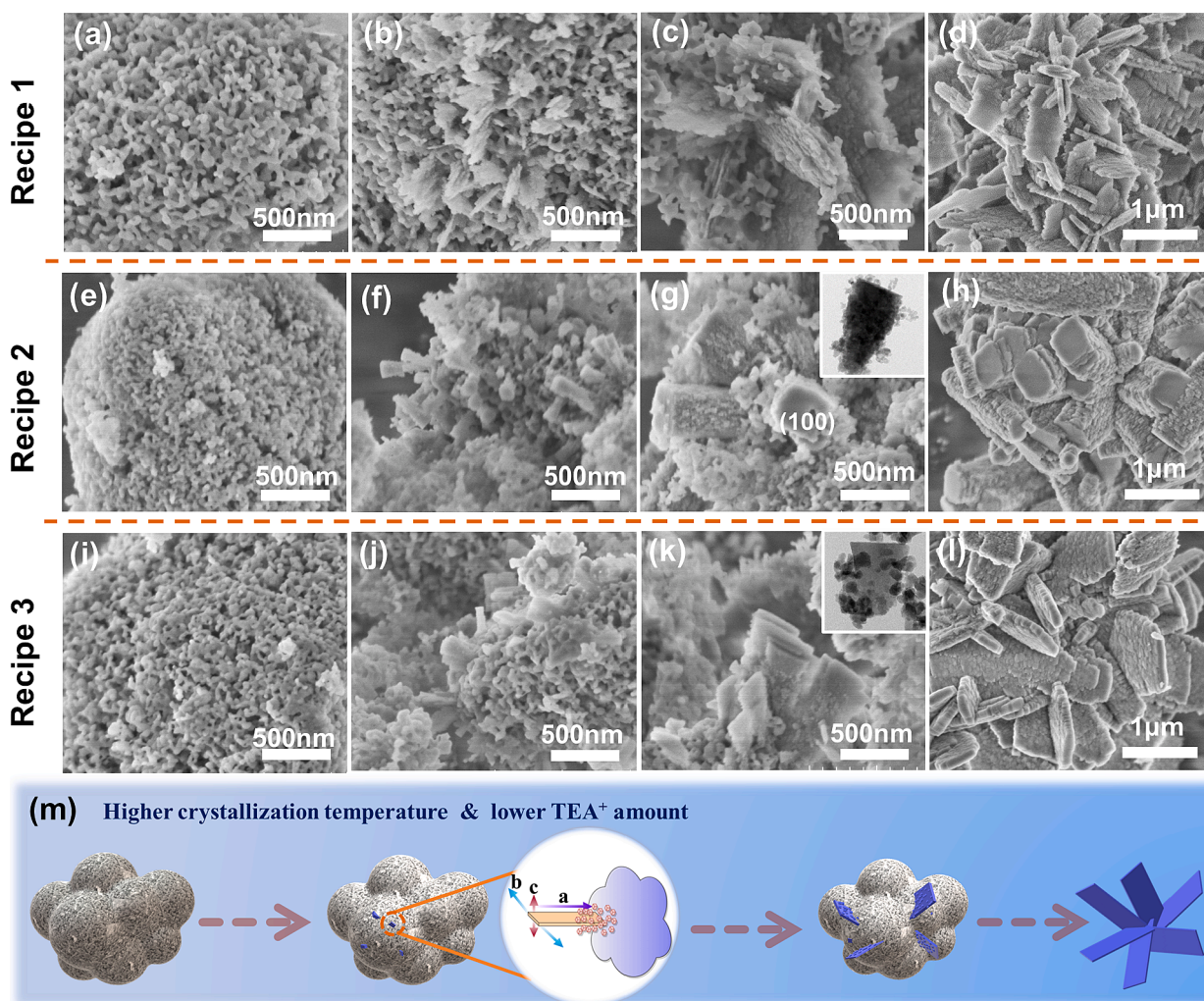


Fig. 3. SEM images of the MOR products at different crystallization stages. (a-d) Recipe 1 for 3 h, 6 h, 9 h and 12 h; (e-h) Recipe 2 for 4 h, 9 h, 19 h and 24 h; (i-l) Recipe 3 for 4 h, 9 h, 19 h and 30 h. (m) Illustration of the evolution process of MOR nanosheets. The gel molar composition for Recipe 1, 2 and 3 is $1\text{SiO}_2: 1/33\text{Al}_2\text{O}_3: 0.2\text{NaOH}: x\text{TEAOH}: 16.7\text{H}_2\text{O}$ with $x = 0.1$ (190 °C), 0.1 (160 °C) and 0.05 (160 °C), respectively. The arrows in the (m) show the crystal growth direction along the a-, b- and c-axis.

to emerge on the surface of amorphous particles, suggesting that heterogeneous nucleation should be responsible for the formation of crystals. Afterwards, the crystals show preferential growth in the a- and b-axis directions, while the growth in the c-axis direction is rather limited. High-resolution SEM images show that the surface of nanosheets is rough and covered with squamous plates. Also, amorphous particles can be observed to be attached on the surface as well as at the edges of the nanosheets (Fig. 3c and S11). Given the less changed solid yields and solid Si/Al ratios during the crystallization, it is speculated that the nanosheets grow via the addition of amorphous particles. In the later stage of crystallization, the classic pathway of monomer addition may occur owing to Oswald ripening, as deduced from the reduced surface roughness of the final well-crystallized nanosheets[51]. Indeed, previous works on ZSM-5 have revealed that the growth of MFI crystals involves both molecule attachment and particle attachment followed by disorder-to-order transition[51,52].

Compared with Recipe 1, Recipe 2 has a lower crystallization temperature of 160 °C. At the initial stage, slender cylindrical crystals emerge on the amorphous particles with their “tail” rooting in the particles (Fig. 3f). The crystals grow large with no preferential growth in specific direction at the expense of amorphous materials (Fig. 3g). It is noted that the cylindrical crystals have highly coarse surface, except for their smooth “top” belonging to (100) face. A large number of

amorphous nanoparticles can be observed to be attached on the uneven surface (Fig. S12), implying the main growth pathway of the crystals via particle addition. On the whole, the crystal growth behavior of Recipe 2 resembles that of Recipe 1 except for the increased crystal thickness in the c-axis. Recipe 3 is similar to Recipe 2 except for the reduce of TEAOH amount by half. It shows similar crystal growth behavior to Recipe 2 (Fig. 3i-l), but with obviously thin crystal thickness. In addition, the dispersed immature crystals of Recipe 2 and 3 in Fig. S12-S13 present a triangle morphology with larger “top” part than the “tail”, which suggests that the crystal growth extends from the exterior to the interior of amorphous particles along the a-axis direction, leading to the crossed architectures of the final crystals. Based on the collected results, three systems follow similar crystal growth mechanism in spite of their different crystal morphology. The evolution of crystallization process to MOR nanosheets is illustrated in Fig. 3m.

It has been recognized that quaternary amine cations in the gel tend to be adsorbed on crystal surface due to the existence of surface hydroxyls and aluminum sites, which can affect the addition of anionic monomeric/oligomeric species[19,53] and modify the growth rate of crystal surface. Herein, in order to better understand the oriented growth of MOR crystals, theoretical calculations were carried out to investigate the adsorption of TEA^+ cations on different crystal faces. A MOR slab of 96 T was constructed to evaluate the binding energy (ΔE)

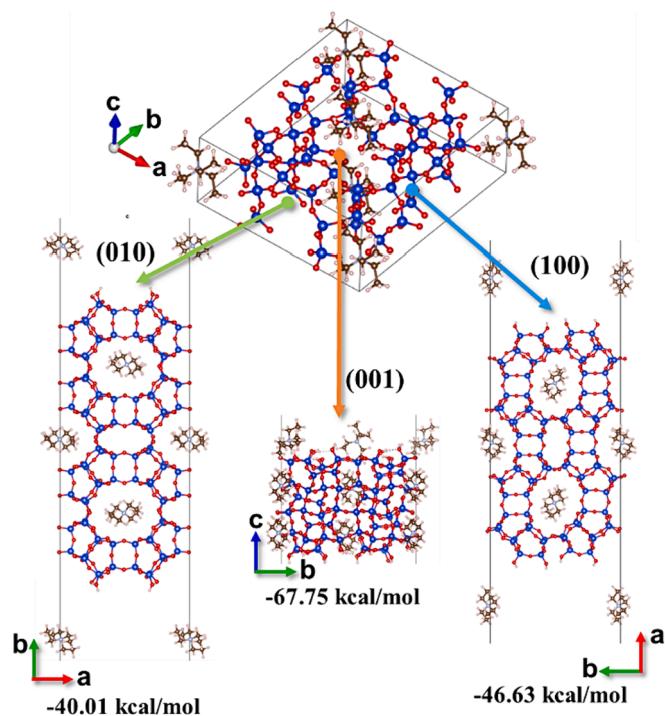


Fig. 4. TEA⁺ distributions in 96 T MOR slabs of (100), (001) and (010) faces and the corresponding binding energies between MOR slabs and TEA⁺.

between TEA⁺ and different faces (see Supporting Information for details). The models of TEA⁺ distribution in MOR slab and the corresponding ΔE are shown in Fig. 4 and Table S7, respectively. The interaction strength between TEA⁺ and the (001) face is obviously stronger than that of TEA⁺ with (010) or (100) faces, as indicated by the more negative ΔE on (001) face. This suggests a preferential adsorption of TEA⁺ on (001) face, which is suspected to reduce the concentration of inorganic sources therein and impede the growth of the crystal face. Moreover, as shown in Fig. S14, the interaction strength increases with the incremental thickness of MOR (001) slab, implying a detrimental effect of TEA⁺ adsorption on the growth of (001) crystal face. As the stronger interaction between TEA⁺ and the (001) face, the density of TEA⁺ adsorbed on (001) face is less affected by the TEA⁺ concentration and temperature changes of the gel, compared with the other two crystal faces. Therefore, when reducing the OSDA dosage or increasing the crystallization temperature, the decrease of TEA⁺ density on (001) faces is expected to be smaller than on other faces, which leads to relatively slow growth rate of (001) face and thus the formation of nanosheets morphology with short c-axis thickness (Fig. S15).

3.3. Application of the strategy in the c-axis thickness tuning of large-pore zeolites

Inspired by the above results that the tunable thickness of MOR crystals along the c-axis arises from the difference in binding energies between TEA⁺ and different crystal faces, it is supposed that the present strategies might be applicable for morphology control of MOR templated by other OSDAs. Herein, we show that the crystal thickness of zeolite MOR can be modified when using hexamethylenimine (HMI) as an OSDA. From Fig. S16, c-axis oriented MOR nanosheets are achieved by adjusting the crystallization temperature. Furthermore, the strategies are also found to be effective for the thickness control of 12-MR channels of zeolite OFF and SAPO-5, as evidenced by the results shown in Table S8 and Fig. S17-S18.

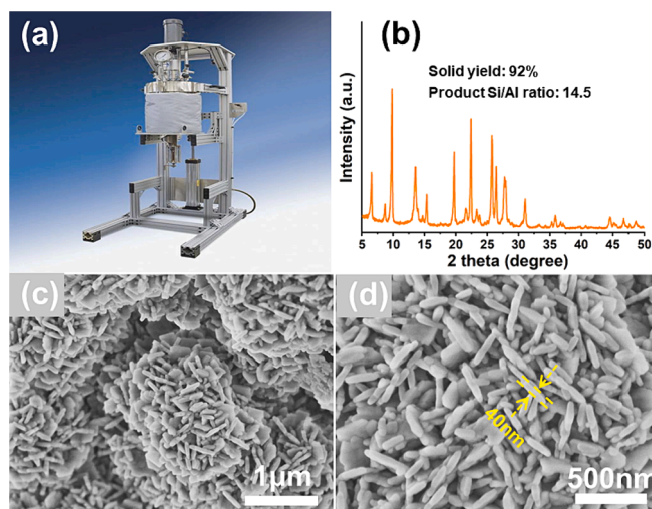


Fig. 5. The scale-up synthesis of MOR-P. (a) Photograph of 10 L Parr autoclave, (b) XRD pattern and (c, d) SEM images of the solid product from 10 L autoclave.

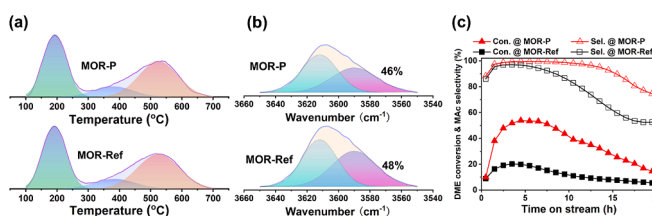


Fig. 6. (a) NH₃-TPD, (b) FTIR spectra of the $\nu(\text{OH})$ vibration region and (c) DME carbonylation performance of H⁺-form MOR-P and MOR-Ref catalysts. Reaction conditions: DME/CO/N₂ = 5/35/60, GHSV = 3600 mL/g/h, 200 °C, 2 MPa.

3.4. Scale-up synthesis of MOR nanosheets

It is well-known that scale-up synthesis of zeolites is important for their practical application, but often full of challenges, especially for the morphology control synthesis. Herein, the scale-up production of MOR-P was performed using a 10 L Parr autoclave. The solid product can be easily separated with the mother liquid and washed with a centrifugation of 5000 rpm. About 1050 g of zeolite powder was finally obtained, corresponding to a high solid yield of ca. 92 %. As shown in Fig. 5, the XRD pattern and SEM image confirm the good crystallinity, purity and nanosheets morphology of the scale-up product, demonstrating the high feasibility of the strategy developed in this work for large-scale production.

3.5. Catalytic performance in DME carbonylation

The nanosheet morphology of zeolite MOR is anticipated to be beneficial for catalytic applications due to the improved mass transfer properties. Herein, the catalytic performances of MOR-P nanosheets in DME carbonylation reactions were investigated. As a comparison, MOR product from Recipe 2 (24 h) was used as the reference (named MOR-Ref). The acid properties of the protonated MOR samples are displayed in Fig. 6a, 6b and Table S9. Two samples possess similar NH₃-TPD profiles, implying their comparable acid strength and acid amounts. The acid amounts with moderate and strong were calculated to be 0.74 and 0.72 mmol/g for MOR-P and MOR-Ref, respectively. The distributions of Brønsted acid sites (BASs) in the 12-MR and 8-MR channels of the samples were investigated by FTIR spectra. On the basis of the deconvolution results of the bridging hydroxyl groups (Fig. 6b), the proportions of BASs in the 8-MR side pocket of MOR-P and MOR-Ref

were 46 % and 48 %, respectively. These results demonstrate that the MOR-P and MOR-Ref possess similar acid properties, including acid amounts and acid distribution.

Fig. 6c displays the DME conversion and methyl acetate (MAc) selectivity of the MOR catalysts as a function of time-on-stream. MOR-P exhibits much better reaction activity and catalyst stability. The highest conversion on MOR-P is 47 %, in sharp contrast with 19 % for MOR-Ref. Meanwhile, the reaction period with MAc selectivity higher than 90 % lasts for 13 h on the former catalyst, but just 6 h on MOR-Ref. The corresponding amount of DME converted on MOR-P is about 5.5 times larger than on MOR-Ref (22.6 vs 4.1 mmol_{DME}/g_{cat}). After 20 h reaction, the converted DME on MOR-P and MOR-Ref are 58.2 mmol_{DME}/g_{cat} and 19.4 mmol_{DME}/g_{cat} respectively. Additionally, the spent catalysts after 20 h reaction were measured by TG-DTA and the curves are shown in Fig. S19. The ratio of coke deposits to the converted DME is calculated to be 0.043 g_{coke}/g_{DME} for MOR-P and 0.128 g_{coke}/g_{DME} for MOR-Ref. These results evidence the advantages of the shorter diffusion path along the straight channel of MOR nanosheets, which reduces the diffusion limitation, alleviates the occurrence of side reactions and abates the blockage of by-products in the channels.

4. Conclusions

A facile strategy has been developed to tailor the anisotropic growth of MOR zeolite without the assistance of mesoporegens and additional modifiers. Both crystallization temperature and TEOH concentration are revealed to be key factors in tuning the c-axis thickness of MOR crystals in the developed system. Higher temperature and lower TEOH concentration can help retard the crystal growth in the c-axis direction, yielding MOR nanosheets product (~40 nm). Theoretical calculations reveal that TEA⁺ has stronger interaction with the (001) face than with other crystal faces, which impedes the growth in the c-axis direction and thus leads to the nanosheets morphology under optimized conditions. The obtained MOR nanosheets behave obviously enhanced catalytic performance in DME carbonylation reaction owing to their short 12-MR diffusion path. The facile strategy together with its successful scale-up synthesis offers a prospect for the production and application of highly efficient MOR nanosheets.

CRedit authorship contribution statement

Kaipeng Cao: Writing – review & editing, Writing – original draft, Visualization, Software, Methodology, Investigation, Formal analysis, Data curation. **Wei Chen:** Writing – review & editing, Software, Formal analysis. **Dong Fan:** Writing – review & editing, Formal analysis, Conceptualization. **Zhenghao Jia:** Formal analysis. **Nan Chen:** Validation. **Dali Zhu:** Validation. **Shutao Xu:** Writing – review & editing. **Anmin Zheng:** Writing – review & editing, Software, Formal analysis. **Peng Tian:** Writing – review & editing, Supervision, Methodology, Funding acquisition, Conceptualization. **Zhongmin Liu:** Writing – review & editing, Supervision, Methodology, Conceptualization.

Declaration of competing interest

The authors declare that they have no known competing financial interests or personal relationships that could have appeared to influence the work reported in this paper.

Data availability

Data will be made available on request.

Acknowledgements

This work is supported by National Natural Science Foundation of China (No. 22288101, 21991090, 21991091, 22272173 and 21676262)

and funding from the Sino-French IRN (International Research Network).

Appendix A. Supplementary data

Supplementary data to this article can be found online at <https://doi.org/10.1016/j.cej.2024.150344>.

References

- [1] J. Liang, G. Shan, Y. Sun, Catalytic fast pyrolysis of lignocellulosic biomass: critical role of zeolite catalysts, *Renew. Sustain. Energy Rev.* 139 (2021), <https://doi.org/10.1016/j.rser.2021.110707>.
- [2] Y. Wu, B.M. Weckhuysen, Separation and purification of Hydrocarbons with porous materials, *Angew. Chem. Int. Ed.* 60 (35) (2021) 18930–18949, <https://doi.org/10.1002/anie.202104318>.
- [3] J. Shi, Y. Wang, W. Yang, Y. Tang, Z. Xie, Recent advances of pore system construction in zeolite-catalyzed chemical industry processes, *Chem. Soc. Rev.* 44 (24) (2015) 8877–8903, <https://doi.org/10.1039/c5cs00626k>.
- [4] A. Inayat, I. Knoke, E. Spiecker, W. Schwieger, Assemblies of mesoporous FAU-type zeolite nanosheets, *Angew. Chem. Int. Ed.* 51 (8) (2012) 1962–1965, <https://doi.org/10.1002/anie.201105738>.
- [5] K. Na, C. Jo, J. Kim, K. Cho, J. Jung, Y. Seo, R.J. Messinger, B.F. Chmelka, R. Ryoo, Directing zeolite structures into Hierarchically nanoporous architectures, *Science* 333 (6040) (2011) 328–332, <https://doi.org/10.1126/science.1204452>.
- [6] M. Moliner, C. Martinez, A. Corma, Multipore zeolites: synthesis and catalytic applications, *Angew. Chem. Int. Ed.* 54 (12) (2015) 3560–3579, <https://doi.org/10.1002/anie.201406344>.
- [7] F. Jiao, X. Pan, K. Gong, Y. Chen, G. Li, X. Bao, Shape-selective zeolites promote ethylene formation from syngas via a ketene intermediate, *Angew. Chem. Int. Ed.* 57 (17) (2018) 4692–4696, <https://doi.org/10.1002/anie.201801397>.
- [8] A. Bhan, A.D. Allian, G.J. Sunley, D.J. Law, E. Iglesia, Specificity of sites within eight-membered ring zeolite channels for carbonylation of methyls to acetyls, *J. Am. Chem. Soc.* 129 (16) (2007) 4919–4924, <https://doi.org/10.1021/ja070094d>.
- [9] S. van Donk, J.H. Bitter, A. Verberckmoes, M. Versluijs-Helder, A. Broersma, K. P. de Jong, Physicochemical characterization of porous materials: spatially resolved accessibility of zeolite crystals, *Angew. Chem. Int. Ed.* 44 (9) (2005) 1360–1363, <https://doi.org/10.1002/anie.200460966>.
- [10] P. Losch, A.B. Pinar, M.G. Willinger, K. Soukup, S. Chavan, B. Vincent, P. Pale, B. Louis, H-ZSM-5 zeolite model crystals: structure-diffusion-activity relationship in methanol-to-olefins catalysis, *J. Catal.* 345 (2017) 11–23, <https://doi.org/10.1016/j.jcat.2016.11.005>.
- [11] K. Cao, D. Fan, S. Zeng, B. Fan, N. Chen, M. Gao, D. Zhu, L. Wang, P. Tian, Z. Liu, Organic-free synthesis of MOR nanoassemblies with excellent DME carbonylation performance, *Chin. J. Catal.* 42 (9) (2021) 1468–1477, [https://doi.org/10.1016/S1872-2067\(20\)63777-9](https://doi.org/10.1016/S1872-2067(20)63777-9).
- [12] J. Zhu, Y. Zhu, L. Zhu, M. Rigutto, A. van der Made, C. Yang, S. Pan, L. Wang, L. Zhu, Y. Jin, Q. Sun, Q. Wu, X. Meng, D. Zhang, Y. Han, J. Li, Y. Chu, A. Zheng, S. Qiu, X. Zheng, F.-S. Xiao, Highly mesoporous single-crystalline zeolite Beta synthesized using a Nonsurfactant cationic Polymer as a dual-function template, *J. Am. Chem. Soc.* 136 (6) (2014) 2503–2510, <https://doi.org/10.1021/ja411117y>.
- [13] J. Perez-Ramirez, C.H. Christensen, K. Egeblad, C.H. Christensen, J.C. Groen, Hierarchical zeolites: enhanced utilisation of microporous crystals in catalysis by advances in materials design, *Chem. Soc. Rev.* 37 (11) (2008) 2530–2542, <https://doi.org/10.1039/b809030k>.
- [14] D.P. Serrano, J.M. Escola, P. Pizarro, Synthesis strategies in the search for hierarchical zeolites, *Chem. Soc. Rev.* 42 (9) (2013) 4004–4035, <https://doi.org/10.1039/c2cs35330j>.
- [15] W. Cui, D. Zhu, J. Tan, N. Chen, D. Fan, J. Wang, J. Han, L. Wang, P. Tian, Z. Liu, Synthesis of mesoporous high-silica zeolite Y and their catalytic cracking performance, *Chin. J. Catal.* 43 (7) (2022) 1945–1954, [https://doi.org/10.1016/S1872-2067\(21\)64043-3](https://doi.org/10.1016/S1872-2067(21)64043-3).
- [16] L. Tosheva, V.P. Valtchev, Nanozeolites: synthesis, crystallization mechanism, and applications, *Chem. Mater.* 17 (10) (2005) 2494–2513, <https://doi.org/10.1021/cm047908z>.
- [17] H. Dai, Y. Shen, T. Yang, C. Lee, D. Fu, A. Agarwal, T.T. Le, M. Tsapatsis, J. C. Palmer, B.M. Weckhuysen, P.J. Dauenhauer, X. Zou, J.D. Rimer, Finned zeolite catalysts, *Nat. Mater.* 19 (10) (2020) 1074–+, <https://doi.org/10.1038/s41563-020-0753-1>.
- [18] T. Zhou, D. Zhang, Y. Sun, T. Ji, S. Huang, Y. Liu, Construction of monodispersed single-crystalline hierarchical ZSM-5 nanosheets via anisotropic etching, *J. Energy Chem.* 72 (2022) 516–521, <https://doi.org/10.1016/j.jechem.2022.06.008>.
- [19] A.I. Lupulescu, M. Kumar, J.D. Rimer, A facile strategy to design zeolite L crystals with tunable morphology and Surface architecture, *J. Am. Chem. Soc.* 135 (17) (2013) 6608–6617, <https://doi.org/10.1021/ja4015277>.
- [20] F. Liu, T. Willhammar, L. Wang, L. Zhu, Q. Sun, X. Meng, W. Carrillo-Cabrera, X. Zou, F.-S. Xiao, ZSM-5 zeolite single crystals with b-Axis-aligned mesoporous channels as an efficient catalyst for conversion of bulky organic molecules, *J. Am. Chem. Soc.* 134 (10) (2012) 4557–4560, <https://doi.org/10.1021/ja300078q>.

- [21] W. Dai, C. Kouvatat, W. Tai, G. Wu, N. Guan, L. Li, V. Valtchev, Platelike MFI crystals with controlled crystal faces aspect ratio, *J. Am. Chem. Soc.* 143 (4) (2021) 1993–2004, <https://doi.org/10.1021/jacs.0c11784>.
- [22] M. Zhai, W. Wu, E. Xing, Y. Zhang, H. Ding, J. Zhou, Y. Luo, J. Liu, K. Zhu, X. Zhu, Generating TON zeolites with reduced 001 length through combined mechanochemical bead-milling and porogen-directed recrystallization with enhanced catalytic property in hydroisomerization, *Chem. Eng. J.* 440 (2022), <https://doi.org/10.1016/j.cej.2022.135874>.
- [23] K. Na, M. Choi, W. Park, Y. Sakamoto, O. Terasaki, R. Ryoo, Pillared MFI zeolite nanosheets of a single-unit-cell thickness, *J. Am. Chem. Soc.* 132 (12) (2010) 4169–4177, <https://doi.org/10.1021/ja908382n>.
- [24] P. Lu, S. Ghosh, M.D. de Mello, H.S. Kamaluddin, X. Li, G. Kumar, X. Duan, M. Abeykoon, J.A. Boscoboinik, L. Qi, H. Dai, T. Luo, S. Al-Thabaiti, K. Narasimharao, Z. Khan, J.D. Rimer, A.T. Bell, P. Dauenhauer, K.A. Mkhoyan, M. Tsapatsis, Few-unit-cell MFI zeolite synthesized using a simple di-quaternary ammonium structure-directing agent, *Angew. Chem. Int. Ed.* 60 (35) (2021) 19214–19221, <https://doi.org/10.1002/anie.202104574>.
- [25] M. Choi, K. Na, J. Kim, Y. Sakamoto, O. Terasaki, R. Ryoo, Stable single-unit-cell nanosheets of zeolite MFI as active and long-lived catalysts, *Nature* 461 (2009) 7265, <https://doi.org/10.1038/nature08493>.
- [26] K. Na, W. Park, Y. Seo, R. Ryoo, Disordered assembly of MFI zeolite nanosheets with a large volume of intersheet mesopores, *Chem. Mater.* 23 (5) (2011) 1273–1279, <https://doi.org/10.1021/cm103245m>.
- [27] J. Jung, C. Jo, K. Cho, R. Ryoo, Zeolite nanosheet of a single-pore thickness generated by a zeolite-structure-directing surfactant, *J. Mater. Chem.* 22 (11) (2012) 4637–4640, <https://doi.org/10.1039/c2jm16539b>.
- [28] P. Cheung, A. Bhan, G.J. Sunley, E. Iglesia, Selective carbonylation of dimethyl ether to methyl acetate catalyzed by acidic zeolites, *Angew. Chem. Int. Ed.* 45 (10) (2006) 1617–1620, <https://doi.org/10.1002/anie.200503898>.
- [29] T. He, G.J. Hou, J.J. Li, X.C. Liu, S.T. Xu, X.W. Han, X.H. Bao, Highly selective methanol-to-olefin reaction on pyridine modified H-mordenite, *Journal of Energy Chemistry* 26 (3) (2017) 354–358, <https://doi.org/10.1016/j.jechem.2017.02.004>.
- [30] Y. Wang, W. Zhou, J. Kang, K. Cheng, S. He, J. Shi, C. Zhou, Q. Zhang, J. Chen, L. Peng, M. Chen, Direct conversion of syngas into methyl acetate, ethanol and ethylene by relay catalysis via dimethyl ether intermediate, *Angew. Chem. Int. Ed.* (2018), <https://doi.org/10.1002/anie.201807113>.
- [31] Z.-J. Zhao, A. Kulkarni, L. Vilella, J.K. Norskov, F. Studt, Theoretical insights into the selective oxidation of methane to methanol in copper-exchanged mordenite, *ACS Catal.* 6 (6) (2016) 3760–3766, <https://doi.org/10.1021/acscatal.6b00440>.
- [32] D.K. Pappas, A. Martini, M. Dyballa, K. Kvande, S. Teketel, K.A. Lomachenko, R. Baran, P. Glatzel, B. Arstad, G. Berlier, C. Lamberti, S. Bordiga, U. Olsbye, S. Svelle, P. Beato, E. Borfecchia, The Nuclearity of the active site for methane to methanol conversion in cu-mordenite: a quantitative assessment, *J. Am. Chem. Soc.* 140 (45) (2018) 15270–15278, <https://doi.org/10.1021/jacs.8b08071>.
- [33] Y. Zhou, J. Zhang, L. Wang, X. Cui, X. Liu, S.S. Wong, H. An, N. Yan, J. Xie, C. Yu, P. Zhang, Y. Du, S. Xi, L. Zheng, X. Cao, Y. Wu, Y. Wang, C. Wang, H. Wen, L. Chen, H. Xing, J. Wang, Self-assembled iron-containing mordenite monolith for carbon dioxide sieving, *Science* 373 (6552) (2021) 315+, <https://doi.org/10.1126/science.aax5776>.
- [34] Y. Wu, S. Zeng, D. Yuan, J. Xing, H. Liu, S. Xu, Y. Wei, Y. Xu, Z. Liu, Enhanced propene/propane separation by directional decoration of the 12-membered rings of mordenite with ZIF fragments, *Angew. Chem. Int. Ed.* 59 (17) (2020) 6765–6768, <https://doi.org/10.1002/anie.202000029>.
- [35] X. Li, R. Prins, J.A. van Bokhoven, Synthesis and characterization of mesoporous mordenite, *J. Catal.* 262 (2) (2009) 257–265, <https://doi.org/10.1016/j.jcat.2009.01.001>.
- [36] K.P. Cao, D. Fan, M.B. Gao, B.H. Fan, N. Chen, L.Y. Wang, P. Tian, Z.M. Liu, Recognizing the important role of Surface Barriers in MOR zeolite catalyzed DME Carbonylation reaction, *ACS Catal.* 12 (1) (2022) 1–7, <https://doi.org/10.1021/acscatal.1c04966>.
- [37] M. Liu, W. Jia, J. Li, Y. Wang, S. Ma, H. Chen, Z. Zhu, Catalytic properties of Hierarchical mordenite nanosheets synthesized by self-assembly between subnanocrystals and organic templates, *Catal. Lett.* 146 (1) (2016) 249–254, <https://doi.org/10.1007/s10562-015-1632-2>.
- [38] B.K. Singh, Y. Kim, S.B. Baek, A. Meena, S. Sultan, J.H. Kwak, K.S. Kim, Template free facile synthesis of mesoporous mordenite for bulky molecular catalytic reactions, *J. Ind. Eng. Chem.* 57 (2018) 363–369, <https://doi.org/10.1016/j.jiec.2017.08.044>.
- [39] S.Y. Wang, B. He, R. Tian, C. Sun, R. Dai, X. Li, X. Wu, X. An, X.M. Xie, Synthesis and catalytic performance of hierarchically structured MOR zeolites by a dual-functional templating approach, *J. Colloid Interf. Sci.* (2018) 339–345, <https://doi.org/10.1016/j.jcis.2018.05.053>.
- [40] O.V. Shvets, K.M. Konyshova, M.V. Shamy, M.V. Opanasenko, P.S. Yaremov, C. H. Xiao, X.D. Zou, J. Cejka, Mordenite nanorods and nanosheets prepared in presence of gemini type surfactants, *Catal. Today* 324 (2019) 115–122, <https://doi.org/10.1016/j.cattod.2018.10.043>.
- [41] Z. McHeik, L. Pinard, J. Toufaily, T. Hamieh, T.J. Daou, Synthesis of Hierarchical MOR-type zeolites with improved catalytic properties, *Molecules* 26 (15) (2021), <https://doi.org/10.3390/molecules26154508>.
- [42] Y. Yuan, L. Wang, H. Liu, P. Tian, M. Yang, S. Xu, Z. Liu, Facile preparation of nanocrystal-assembled hierarchical mordenite zeolites with remarkable catalytic performance, *Chin. J. Catal.* 36 (11) (2015) 1910–1919, [https://doi.org/10.1016/s1872-2067\(15\)60960-3](https://doi.org/10.1016/s1872-2067(15)60960-3).
- [43] Y. Xu, X.F. Shen, C. Peng, Y. Ma, L. Han, P. Wu, H.G. Peng, S.N. Che, Synthesis of ultra-small mordenite zeolite nanoparticles, *Sci. China-Mater.* 61 (9) (2018) 1185–1190, <https://doi.org/10.1007/s40843-018-9257-3>.
- [44] M. Kumar, Z.J. Berkson, R.J. Clark, Y. Shen, N.A. Prisco, Q. Zheng, Z. Zeng, H. Zheng, L.B. McCusker, J.C. Palmer, B.F. Chmelka, J.D. Rimer, Crystallization of mordenite platelets using cooperative organic structure-directing agents, *J. Am. Chem. Soc.* (2019), <https://doi.org/10.1021/jacs.9b09697>.
- [45] K. Lu, J. Huang, L. Ren, C. Li, Y. Guan, B. Hu, H. Xu, J. Jiang, Y. Ma, P. Wu, High ethylene selectivity in methanol-to-olefin (MTO) reaction over MOR-zeolite nanosheets, *Angew. Chem. Int. Ed.* 59 (15) (2020) 6258–6262, <https://doi.org/10.1002/anie.202000269>.
- [46] M. Ma, X. Huang, E. Zhan, Y. Zhou, H. Xue, W. Shen, Synthesis of mordenite nanosheets with shortened channel lengths and enhanced catalytic activity, *J. Mater. Chem. A* 5 (19) (2017) 8887–8891, <https://doi.org/10.1039/c7ta02477k>.
- [47] S. Li, J. Li, M. Dong, S. Fan, T. Zhao, J. Wang, W. Fan, Strategies to control zeolite particle morphology, *Chem. Soc. Rev.* 48 (3) (2019) 885–907, <https://doi.org/10.1039/c8cs00774h>.
- [48] J.P. Perdew, K. Burke, M. Ernzerhof, Generalized gradient approximation made simple, *Phys. Rev. Lett.* 77 (18) (1996) 3865–3868, <https://doi.org/10.1103/PhysRevLett.77.3865>.
- [49] S. Grimme, J. Antony, S. Ehrlich, H. Krieg, A consistent and accurate ab initio parametrization of density functional dispersion correction (DFT-D) for the 94 elements H-pu, *J. Chem. Phys.* 132 (15) (2010), <https://doi.org/10.1063/1.3382344>.
- [50] B. Delley, From molecules to solids with the DMol(3) approach, *J. Chem. Phys.* 113 (18) (2000) 7756–7764, <https://doi.org/10.1063/1.1316015>.
- [51] A.I. Lupulescu, J.D. Rimer, In situ imaging of Silicalite-1 Surface growth reveals the mechanism of crystallization, *Science* 344 (6185) (2014) 729–732, <https://doi.org/10.1126/science.1250984>.
- [52] Z. Sheng, H. Li, K. Du, L. Gao, J. Ju, Y. Zhang, Y. Tang, Observing a zeolite nucleus (subcrystal) with a uniform framework structure and its oriented attachment without single-molecule addition, *Angew. Chem. Int. Ed.* 60 (24) (2021) 13444–13451, <https://doi.org/10.1002/anie.202102621>.
- [53] K.E. Jelfs, B. Slater, D.W. Lewis, D.J. Willock, The role of organic templates in controlling zeolite crystal morphology, 15th international zeolite conference, PEOPLES R CHINA, Beijing, 2007, pp. 1685–1692.